Hindawi
Advances in Materials Science and Engineering
Volume 2023, Article ID 9865245, 1 page
https://doi.org/10.1155/2023/9865245

Retraction

Retracted: Fabrication of Hollow Needle Tips with Nanoholes by Plasma Maskless Processing and Calculation and Detection of Complex Surface Edges

Advances in Materials Science and Engineering

Received 26 December 2023; Accepted 26 December 2023; Published 29 December 2023

Copyright © 2023 Advances in Materials Science and Engineering. This is an open access article distributed under the Creative Commons Attribution License, which permits unrestricted use, distribution, and reproduction in any medium, provided the original work is properly cited.

This article has been retracted by Hindawi, as publisher, following an investigation undertaken by the publisher [1]. This investigation has uncovered evidence of systematic manipulation of the publication and peer-review process. We cannot, therefore, vouch for the reliability or integrity of this article.

Please note that this notice is intended solely to alert readers that the peer-review process of this article has been compromised.

Wiley and Hindawi regret that the usual quality checks did not identify these issues before publication and have since put additional measures in place to safeguard research integrity.

We wish to credit our Research Integrity and Research Publishing teams and anonymous and named external researchers and research integrity experts for contributing to this investigation.

The corresponding author, as the representative of all authors, has been given the opportunity to register their agreement or disagreement to this retraction. We have kept a record of any response received.

References

[1] Z. Dai, S. Zhou, T. Yang, and Y. Wang, "Fabrication of Hollow Needle Tips with Nanoholes by Plasma Maskless Processing and Calculation and Detection of Complex Surface Edges," *Advances in Materials Science and Engineering*, vol. 2022, Article ID 1113658, 11 pages, 2022.

Hindawi
Advances in Materials Science and Engineering
Volume 2022, Article ID 1113658, 11 pages
https://doi.org/10.1155/2022/1113658

RETRACTED

Research Article

Fabrication of Hollow Needle Tips with Nanoholes by Plasma Maskless Processing and Calculation and Detection of Complex Surface Edges

Zuocai Dai, [1,2] Sha Zhou, [3] Tongguang Yang, [1,2] and Yanpeng Wang [1]

[1] *College of Mechanical and Electrical Engineering, Hunan City University, Yiyang 413002, Hunan, China*
[2] *Key Laboratory Energy Monitoring and Edge Computing for Smart City of Hunan Province, Yiyang 413002, Hunan, China*
[3] *Hunan City University, Yiyang 413002, Hunan, China*

Correspondence should be addressed to Zuocai Dai; daizuocai@hncu.edu.cn

Received 18 May 2022; Revised 25 July 2022; Accepted 1 August 2022; Published 14 September 2022

Academic Editor: Haichang Zhang

Copyright © 2022 Zuocai Dai et al. This is an open access article distributed under the Creative Commons Attribution License, which permits unrestricted use, distribution, and reproduction in any medium, provided the original work is properly cited.

The plasma maskless processing method combines the advantages of plasma etching and scanning probe processing, such as high etching efficiency, wide range of applicable materials, and high resolution. This method is based on the probe driving and detection of piezoelectric thin films, which enables all probes in the array to be processed completely independently, greatly improving the overall processing efficiency, and can effectively etch specific nano-scale regions of various materials. And it provides an effective solution for efficiently processing small batches of multi-variety micro-nano devices. In this study, a hollow needle tip with nanoholes was fabricated by plasma maskless processing, and use edge computing to calculate the complex surface shape of the needle tip. By establishing a plasma reactor, using the calculation method of the complex surface edge of the needle tip, and testing the stability of the processed nanotip by means of filling air pressure and power excitation in the experiment. The results show that when the breakdown voltage SF6 discharges, with the increase of air pressure, the breakdown voltage of the arrester first decreases and then increases gradually, and it is the smallest at 5 kPa and reaches the optimal 490 V, (PD) $m = 0.5$ Pa·m. And the Ar reaction ionization potential (15.76 eV) and excitation potential (11.53 eV, 11.72 eV) are lower than the splitting potential (≥16 eV) of SF6. As time goes on, high-energy particles are neutralized with the vessel wall, so the ion concentration is gradually smaller, sparse between 200 and 250, and increases from 100 to 300, which is close to the peak value, according to the gradual increase of the discharge voltage. The data obtained from the experimental test proves the reliability of the nanotips prepared in this study, and the properties remain stable under different breakdown voltages. Therefore, the nanohole hollow tip processed by maskless scanning plasma in this study has reached the standard of process use and has important application significance.

1. Introduction

In recent years, plasma has been used as a new source for maskless etching of material surfaces, and it has received extensive attention from scholars all over the world because of its good application potential. There are mainly two forms of micro-plasma maskless etch structures reported in the current literature, one is the thin-film micro-electrode structure, and the other is the plasma micro-spray structure. The main disadvantage of the two is that the etching pattern precision is not high (usually tens of micrometers to hundreds of micrometers), it is difficult to fabricate in batches, and it is not suitable for processing complex patterns. The plasma maskless etching system used in this study is modified on the basis of the existing market, is modified to meet the needs of preparing nano-hollow needle tips in this study, and overcome the shortcomings of being unsuitable for processing complex patterns.

Edge computing adopts a distributed computing architecture, and the operations of applications, data, and services previously processed by the network center node are processed by the edge nodes on the network logic. Edge

computing decomposes large services into smaller and easier-to-manage parts, and distributes large services that were originally handled entirely by central nodes to edge nodes. The edge node is closer to the user terminal device, which significantly improves the data processing speed and transmission speed, and further reduces the delay.

Complex surface shape refers to non-rotationally symmetric parts or surface contours with complex asymmetric structures, which are difficult to express with unified mathematical formulas. These parts are often critical parts of the system and have unique roles. At present, the processing methods of complex surface structure parts include grinding and polishing, etching, X-ray lithography mask, molding, and so on. However, the methods of processing complex surface shapes on the market each have their own defects or limitations of use. The innovation of this study is mainly reflected in two aspects: 1. In the process of processing, the discharger is integrated on the scanning probe of the hollow needle tip of the nanohole. At present, the inverted pyramid micro-discharger has a simple structure. Here, the inverted-pyramid micro-discharger is integrated into a scanning probe with a hollow needle tip, and nano-scale micropores are released at the tip of the discharger. 2. The main component of the discharge gas is SF6. At present, the discharge gases of micro-dischargers are mostly rare gases such as Ar and Ne, and SF6 is very rare in the fabrication of nanohole hollow needle tips. Because it has the advantages of good selectivity, high etching efficiency, and no carbon deposits on the etching surface in the etching process, we choose SF6 as the reactive gas in the micro-discharger. Using its etching characteristics to complete this production, it also provides a reference for the gas selection for the preparation of other similar materials.

2. Related Work

Plasma etching technology has been widely used due to its high etching rate, good directionality, and material selectivity. In wafer fabrication, Wan proposed a dry plasma maskless etching process for the construction of aluminum interconnect structures [1]. In recent years, as the geometry of chips has become smaller and smaller, the width of Al wiring specifications has also been shrinking. In order to print smaller geometries, the thickness in the mask process must also be reduced for better resolution, which creates challenges for the plasma etching process and requires newer equipment to perfect. Shimizu et al. used plasma maskless etching to fabricate silicon patterns, and successfully produced good spatial patterns with a width of about 0.2 μm through the "reverse patterning process" [2]. However, the roughness of the line edge is large, which makes this technology need more refined technology to improve. Because the complex surface shape is complex and difficult to operate, Wang et al. introduced a new method to control the forming defects of the complex surface shape, introducing edge and notch cutting to solve the forming defects and reduce the number of stamping tools [3]. However, his method is difficult to be uniformly applicable to different models, and cannot be applied in batches. Sosin et al. are committed to developing the calculation algorithm of the grid method, which is used to study the interaction between shock waves and moving bodies with piecewise linear boundaries, so as to play an inference role in the calculation and research of complex surface shapes. However, his algorithm is too complicated, and it is difficult to achieve excellent processing results in the infrequent calculation method [4]. Tang et al. proposed a localized approximation method using polynomial basis functions to solve the plate bending problem with complex surface shapes. To alleviate the difficulty of solving the fourth-order plate bending problem using local configuration methods, additional methods are introduced outside the computational domain to improve stability and accuracy [5]. However, the method proposed by him is also partial to the problem of complex surface shape, and cannot complete the production of complex surface shape based on the overall framework. In the field of edge computing, Kochovski and Stankovski developed a practical edge computing architecture and design that can be used to support intelligent construction environments with high QoS, with special attention to solution design, which has strong practicability [6]. However, this technology relies on the latest cloud and software engineering methods and technologies, so it has short-term disadvantages and cannot be used for long-term use. Tran et al. proposed an edge real-time computing, context-aware collaboration framework, including MEC servers and mobile devices, and integrated heterogeneous resources at the edge. This approach relieves the backhaul and core network and is critical for enabling low-latency, high-bandwidth, and agile mobile services [7]. However, in terms of operation speed, the calculation method he proposed is still slightly lacking, and it is easy to be replaced by other more efficient algorithms, so more improvements are needed.

3. Plasma Maskless Processing of Nano-Hole Hollow Tip and Detection Method

Plasma is a basic form of matter, and its components include: positive ions, negative ions, electrons, free radicals and various activist groups, etc. These components are generally positive and negative in terms of electricity, so they are macroscopically neutral, so they are called plasma [8]. Common plasmas and their applications in life are: the sun, lightning, neon lights, plasma welding, etc. In order to understand what plasma is, people can understand its generation mechanism from the three-state change of matter. When a solid substance is heated from a low temperature, the substance will gradually melt from a solid state to a liquid state, and then evaporate into a gaseous state. At this time, if the heating continues to a certain extent, the gas will develop to the plasma state, so the plasma is also called the fourth state of matter [9]. Figure 1 is a schematic diagram of the process.

Plasma is fundamentally different from the other three states in structure, composition, and properties. It is a conductive fluid as a whole and there is a Coulomb force between its constituent particles [10]. These differences give plasma certain properties, such as plasma oscillations and

RETRACTED

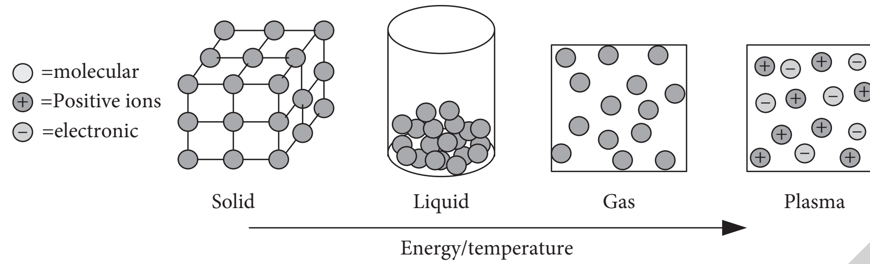

FIGURE 1: Schematic diagram of the plasma formation process.

RETRACTED

plasma radiation. The classification of plasmas according to their mode of existence and their thermodynamic equilibrium is shown in Table 1.

3.1. Basic Structure Model of Microplasma Reactor. Before processing the nanohole hollow tip, a method for plasma maskless body processing should be constructed first. Figure 2 is a schematic structural diagram of the maskless plasma etching processing unit in this study. The system mainly includes three main parts: a tiny plasma reactor, a hollow needle tip and a scanning probe with a piezoelectric drive.

Selecting corresponding reactive gases for different materials to be processed can effectively etch specific nanoscale regions of various materials. The probe drive and detection based on piezoelectric film will enable all probes in the array to be processed completely independently, greatly improving the overall processing efficiency [11]. In addition, this method separates the etching device from the material to be etched, and the etching system is relatively simple. And it can achieve nanometer-scale high-precision etching, which is of great significance for the research of localized plasma etching, and provides an effective solution for the efficient processing of micro-nano-hole hollow tips [12].

The scanning plasma processing system can be broken down into three key basic parts according to its structure. Among them, the microplasma reactor is one of the key devices for generating and maintaining plasma in the system, and the research on its performance and principle is also the key content to realizing the preparation of the whole system [13]. Microplasma reactor is the key device for generating plasma, and its performance plays a pivotal role in the entire etching system.

The inverted pyramid micro-plasma reactor here is a discharge device used for maskless scanning plasma etching, so it is necessary to integrate the micro-discharger into the tip of the scanning probe. Nickel (Ni) was chosen as the electrode metal for the microplasma reactor. This is because the chemical properties of Ni are relatively stable and do not interact with elements such as oxygen, sulfur, and chlorine. It has excellent etching resistance in CHFg and SF plasma, and at the same time, it has high melting point and low sputtering yield, is cheap, and also meets the requirements for electrode materials during plasma discharge. The design thickness of the electrode layer is 120–200 nm. Polyimide (PI) material is selected as the material for the intermediate insulating layer of the reactor, because this material has superior dielectric properties, mechanical properties and thermal stability, and is one of the ideal materials for high-temperature electrical and thermal insulation. PI has good corrosion resistance in SF plasma, excellent high-temperature performance, simple processing technology, low manufacturing cost, low relative permittivity, and good insulating properties.

3.2. Calculation of Complex Surface Shape Edge of Maskless Etched Tip. Before processing with a plasma processing system, the first step is to measure the effect of current density on electroplating, and the most important step in this step is the calculation of the thickness of the nickel layer. Because people use a constant current during the electroplating process, the current density is generally between 5. According to the required thickness of the nickel layer, people generally choose a time of about two hours.

A current density of J = 15mA/*c* was chosen to calculate the thickness of the nickel layer obtained by electroplating. Then by the formula:

$$J = \mathrm{I}\bullet\mathrm{s},\qquad \mathrm{Q} = \mathrm{I}\bullet\mathrm{t}. \tag{1}$$

The size of the number of charges in two hours can be obtained, then people can use the formula:

$$\mathrm{N_e} = \frac{Q}{q}. \tag{2}$$

The number of electrons can be obtained, and then by the formula:

$$\mathrm{n}_e = \frac{N_e}{N_{av}}. \tag{3}$$

According to the chemical coefficient table, we can find that the molar mass of Ni is 48.7 g/mol, so the mass in two hours can be obtained as

$$\mathrm{m} = n\bullet 48.7. \tag{4}$$

The density of Ni is 8.9 g/mol, then the volume of Ni displaced is

$$\mathrm{V} = \frac{\mathrm{m}}{\mathrm{p}}. \tag{5}$$

Finally by the formula

Table 1: Classification of plasma.

Categorization	High-temperature plasma	Low temperature plasma	
		Thermal plasma	Cold plasma
Temperature range	10^6-10^8K	10^3-10^5K	10^2-10^5K
Thermodynamic properties	Thermodynamic equilibrium	Thermodynamic equilibrium or near thermodynamic equilibrium	Non-thermodynamic equilibrium
Instances	Plasma-controlled thermonuclear fusion on the sun	High frequency plasma magnetic fluid discharge	Corona discharge Spark discharge

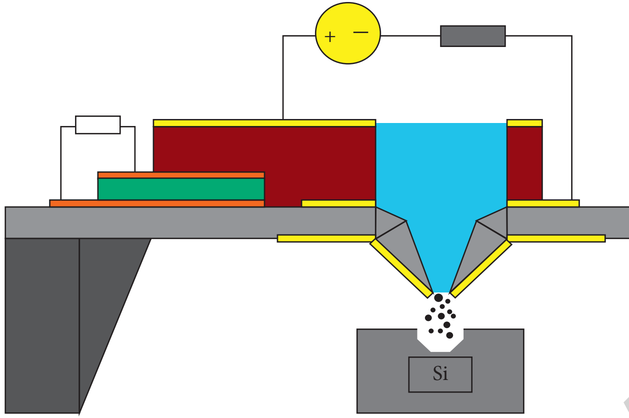

Figure 2: Maskless scanning plasma etching processing unit.

$$H = \frac{V}{s}. \tag{6}$$

The theoretical thickness of the obtained Ni layer is 30.625 microns (where N_{av} is Avogadro's constant 6.02214×10^{23}, and q is the basic charge 1.60218×10^{-19}C). This is a little different from the thickness of the nickel layer we actually plated out. The thickness of the nickel layer actually electroplated is about 25 microns, which is related to the efficiency of the current.

Next, we use the femlab model method to introduce the simulation of the stress when the nano-hollow tip is separated from the silicon-based mold. The principle used in our simulation is that the stress of a material is represented by a relatively symmetrical stress tensor:

$$\sigma = \begin{pmatrix} \sigma_x \tau_{xy} \tau_{xy} \\ \tau_{yx} \sigma_y \tau_{yz} \\ \tau_{zx} \tau_{zy} \sigma_z \end{pmatrix} \tau_{xy} = \tau_{yx} \tau_{xz} = \tau_{zx} \tau_{yz} = \tau_{zy}. \tag{7}$$

The formula contains 3 standard stresses (O_x,O_y ,O_z) and 6 tangential stresses. If it is a symmetric system, there are only three tangential stresses (τ_{xy},τ_{xz},τ_{yz}).

First, since the thermal expansion coefficient of the material used is a linear coefficient. So, we used a model of a linear elastic material. The relational expression of the stress in the linear case or its formula composition includes two parts, the initial stress and the thermal effect, and the relational expression is

$$\sigma = D_{\varepsilon_{el}} + \sigma_0 = D\left(\varepsilon - \varepsilon - \varepsilon_0\right) + \sigma_0. \tag{8}$$

In the formula, D is a 6×6 elastic matrix, and the composition of stress is expressed by an array of vectors defined by the longitudinal vectors of 6 stresses:

$$\sigma = \begin{pmatrix} \sigma_x \\ \sigma_y \\ \sigma_z \\ \tau_{xy} \\ \tau_{yz} \\ \tau_{xz} \end{pmatrix} \varepsilon = \begin{pmatrix} \varepsilon_x \\ \varepsilon_y \\ \varepsilon_z \\ \gamma_{xy} \\ \gamma_{yz} \\ \gamma_{xz} \end{pmatrix}. \tag{9}$$

The definition of the elastic matrix D, or other basic matrices, or the inversion matrix D^{-1} of D varies depending on the material, they differ due to different materials. For example, isotropic materials and anisotropic materials are defined differently. The following is an example of the expression of the D^{-1} matrix of isotropic materials:

$$D^{-1} = \frac{1}{E} \begin{pmatrix} 1 - v - \nu 0 0 0 \\ -v 1 - \nu 0 0 0 \\ -v - v 1 0 0 0 \end{pmatrix}. \tag{10}$$

In this formula, E is the elastic coefficient or Young's modulus, and v is the Poisson coefficient. They define the property of shrinkage in the vertical direction. The result of reversing D^{-1} is

$$D = \frac{E}{(1 + v)(1 - 2\nu)}. \tag{11}$$

In the formula, E is the Young's modulus and v is the Poisson coefficient. In this way, according to σ_0, ε, the result of linear stress σ can be obtained. We defined Ni, Si and SiO_2 as isotropic materials, and adopted this model to verify the principle of needle peeling.

Then, since we are studying the stress change between Ni, Si and SiO_2 after heating and cooling, the model of thermal stress also be chosen. The magnitude of the thermal stress is determined by several variables: the current temperature T, the reference temperature T_{ref} when the thermal stress is zero, and the thermal spread vector a_{vec}. The expression is as follows:

RETRACTED

$$\varepsilon_{\mathrm{th}} = \begin{pmatrix} \varepsilon_x \\ \varepsilon_y \\ \varepsilon_z \\ \gamma_{xy} \\ \gamma_{yz} \\ \gamma_{xz} \end{pmatrix}_{th} = a_{vec}\left(T - T_{ref}\right). \quad (12)$$

The composition of a_{vec} in this formula is different depending on the selected material. For example, the expression of a_{vec} for isotropic materials is

$$a_{vec} = \begin{pmatrix} a \\ a \\ a \\ 0 \\ 0 \\ 0 \end{pmatrix}. \quad (13)$$

In order to study whether the produced needle can pierce the human skin, whether it will break, whether it will break, etc., we used Femlab to simulate these situations. And it is proved that the electroplated Ni hollow microneedle can withstand the pressure brought by piercing the skin without breaking or breaking.

People still first introduce the Femlab model used in the simulation process, its construction process and the meaning of variable expression in it. This model describes the relationship between tension and displacement, which can be fully described by the deformation of the structure and the derived variables of this deformation [14]. This tension can be broken down into three parts: thermal tension ($\varepsilon_{\mathrm{th}}$), initial tension (ε_0), and elastic tension (ε_{el}). The expression is as follows:

$$\varepsilon = \varepsilon_{\mathrm{el}} + \varepsilon_{th} + \varepsilon_0. \quad (14)$$

Since the microneedles penetrate the human skin to a depth of about 100 microns, a small displacement model was chosen for the simulation. This small displacement model assumes that the normal tension components and the tangential tension components are provided by the deformation of the object, as shown in the formulas:

$$\begin{aligned} \varepsilon_x &= \frac{\partial u}{\partial x}\varepsilon_{\mathrm{xy}} = \frac{\gamma_{xy}}{2} = \frac{1}{2}\left(\frac{\partial u}{\partial x} + \frac{\partial v}{\partial x}\right), \\ \varepsilon_y &= \frac{\partial v}{\partial y}\varepsilon_{\mathrm{yz}} = \frac{\gamma_{yz}}{2} = \frac{1}{2}\left(\frac{\partial v}{\partial z} + \frac{\partial w}{\partial y}\right), \\ \varepsilon_z &= \frac{\partial w}{\partial z}\varepsilon_{\mathrm{xz}} = \frac{\gamma_{xz}}{2} = \frac{1}{2}\left(\frac{\partial u}{\partial z} + \frac{\partial w}{\partial x}\right). \end{aligned} \quad (15)$$

4. Experiment and Test of Maskless Etching of Nano-Hollow Tip

4.1. Microplasma Reactor Etching Process. Micro-discharger is a key device in the maskless scanning plasma etching system, which mainly includes a three-layer structure of anode metal/insulation layer/cathode metal. Inverted pyramid microdischargers have feature sizes of 100 μm or 50 μm and groove depths of about 70 μm or 35 μm. The anode metal of the micro-discharger is Ni with a thickness of 200 nm. The insulating layer material is polyimide ZKPI-305 with superior dielectric properties, mechanical properties and thermal stability, with a thickness of 10 μm.

Figure 3 is the general flow of the maskless etching process in the microplasma reactor. First, 1.2 μm thick SiO_2 is obtained by double-sided oxidation of the 100-crystalline silicon wafer. Inverted pyramid windows are etched on the front side, and SiO_2 is etched by reactive ion etching (RIE) to obtain an inverted pyramid etch mask. The inverted pyramid grooves were obtained by wet etching with KOH, and the SiO_2 was removed with hydrofluoric acid. Then double-sided oxidation to obtain a SiO_2 layer. The cathode Ni is then magnetron sputtered and patterned, then a layer of polyimide (ZKPI-305) is coated and cured. Then, the image inversion method was used to strip the process to realize the patterning of the PI etching Ni mask, and then RIE was used to etch the PI. The Ni mask is then patterned to form the upper electrode, then the double-sided SiO_2 is patterned, and the microreactor cantilever will be released. In order to compare the discharge characteristics, a micro-discharger with a planar structure is also designed for comparison. Compared with the inverted pyramid process, the planar discharger does not need to etch the inverted pyramid groove, and the subsequent process is the same. The planar micro-discharger process is relatively simple, and the RIE etch PI process is faster and of better quality [15].

4.2. PI Preparation and Etching Process. During the fabrication of inverted pyramid microdischargers, the patterning of upper and lower electrodes and the preparation and patterning of PI are two important steps that affect the entire process flow and device quality.

At present, the image inversion method is commonly used to strip evaporated metal. Due to the weak coverage of the steps by the evaporated metal, it is very favorable for the peeling of the plane pattern. However, the evaporation film is prone to pinholes and has poor adhesion to the substrate, which cannot meet the requirements of micro-dischargers. The sputter-deposited film is uniform and dense, has good performance, and is firmly attached to the substrate, but it is not conducive to peeling due to its strong step coverage [16]. At present, there have been preliminary studies on the stripping of sputtered metal by the reverse method, but these

RETRACTED

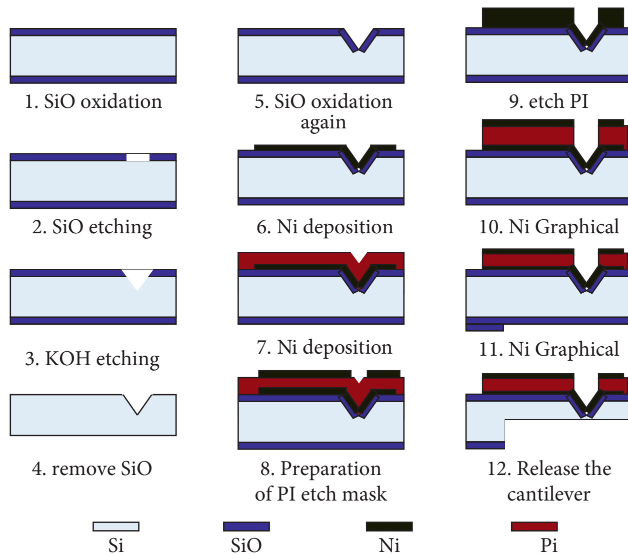

Figure 3: The general flow of the maskless etching process in the microplasma reactor.

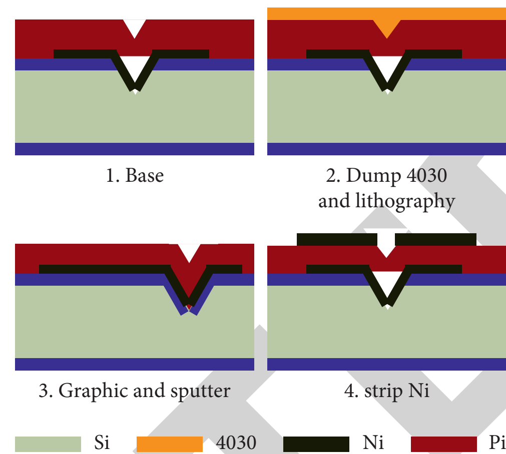

Figure 4: Process flow of electrode patterning on the micro-discharger.

methods are also mostly used for flat patterns, and the micro-discharger needs to strip the metal in the uneven deep groove, which is difficult to achieve. Here, we first study the sputtering reverse lift-off process on the silicon substrate, apply 4030 glue on the silicon substrate, and realize reverse patterning. Then a Ni film was deposited on the silicon substrate by sputtering, and finally the metal was stripped off by soaking in acetone and ultrasonic vibration [17]. On this basis, the electrode patterning on the Ni top of the inverted pyramid micro-discharger is realized by the sputtering reverse lift-off process. Figure 4 is the electrode patterning process flow on the inverted pyramid micro-discharger. First, oxidize both sides of the silicon wafer, lithography the inverted pyramid window on the front, and use KOH wet etching to obtain the inverted pyramid groove, and remove SiO_2 with hydrofluoric acid (HF). Cathode Ni was then sputtered over the entire substrate, coated with a PI insulating layer and cured [18]. Subsequently, 4030 paste was applied and reverse patterned on the PI, then the anodic Ni film was sputter deposited and stripped, and finally, the PI was etched with RIE.

4.3. Influence of Ni Sputter Coating Conditions on Peeling. In the sputtering reversal lift-off process, factors such as sputtering power and time, sample heating, and acetone ultrasonic vibration cleaning have a great influence on the quality, thickness, and lift-off of the Ni film. Table 2 shows the relevant parameters of Ni film peeling. The experimental results and analysis are:

The sputtering time has a certain influence on the thickness of the Ni film. Figure 5 shows the relationship between the thickness of Ni film and time when the sputtering power is 80 w. It can be seen from the figure that the thickness of the Ni film and the sputtering time are basically linear, and the thickness of the Ni film is about 200 nm when the sputtering time is 80 min, which has reached the thickness of the electrode layer for the normal operation of the microreactor. The peeling can still be achieved after sputtering for 99 min, and the thickness of the Ni film reaches 230 nm. Sputtering is a process in which Ar plasma bombards the target material to make Ni particles detached from the deposition. When the power, airflow, and other conditions are kept constant during sputtering, increasing the time will inevitably increase the film thickness [19].

In order to avoid too large overlapping area of the upper cathode and increase the defect discharge. Firstly, the process is adjusted, that is, the cathode is patterned first, so that it only has a three-layer structure of electrode/insulation layer/electrode at the cantilever beam. The bottom electrode patterning can be realized by the wet etching method, and the obtained metal quality is good, but the wet etching process is relatively complicated, and it is easy to cause pollution of metal ions [20]. In order to simplify the process and improve the metal quality, the 4450 negative adhesive stripping process is used here to realize the patterning of the lower electrode.

Figure 6 is the flow chart of the lower electrode stripping process of inverted pyramid micro-discharger. First, the 4450 negative photoresists is coated on the silicon substrate engraved with the inverted pyramid and patterned by one mask exposure and development. Metallic Ni was then sputtered and exfoliated using acetone sonication. As can be seen from the flow chart, the 4450 photoresist in the inverted pyramid is not directly removed by light, which is the characteristic of the negative photoresist itself, so its removal ability will not be affected by the increase in thickness.

Since the stripping process of the lower electrode has many similarities with the stripping process of the upper electrode, and is obviously simpler than the flipping and stripping process of the upper electrode, the specific research content of the performance of the 4450 glue and the metal sputtering process and parameters will not be repeated here.

4.4. Influence of Sputter Coating Conditions on Peeling. Making PI films with good surface quality and excellent performance is also a crucial process in maskless etching.

RETRACTED

Table 2: Ni film stripping process parameters and thickness.

Sputtering power(w)	120	100	0	80	0	0	0	0
Sputtering time (min)	30	40	60	40	50	60	80	99
Film thickness (nm)	90	130	160	90	130	140	200	230
Ultrasonic wash time (s)	Not stripped	20	Partly stripped	10	20	60	30	10

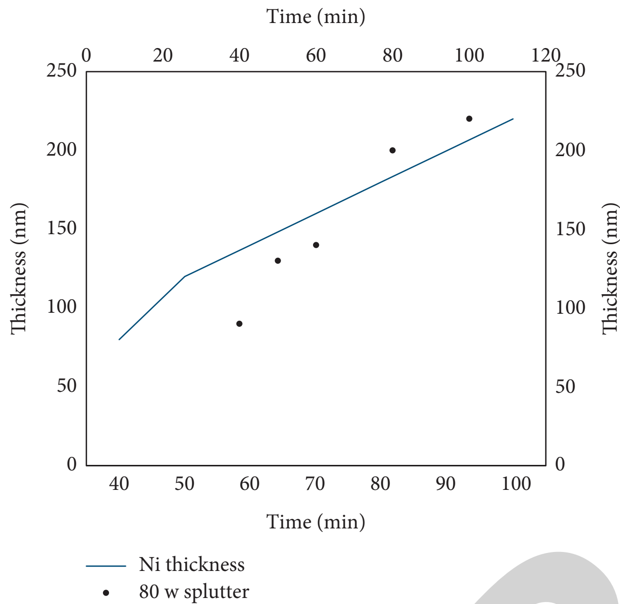

Figure 5: Relationship between Ni thickness and time of 80 w sputtering.

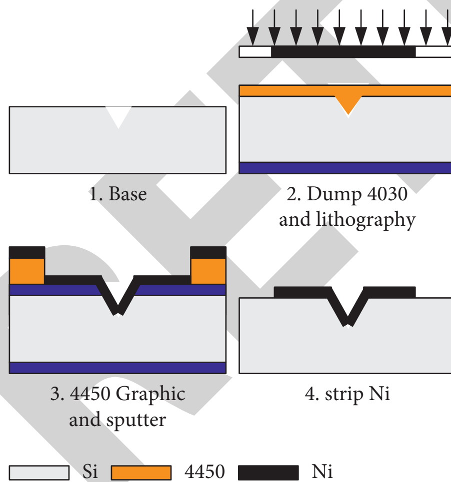

Figure 6: Process flow of the lower electrode of the micro-discharger.

The PI process generally includes preparation and patterning steps. Improper handling will cause problems such as cracks and residues, which will affect its quality and performance [21]. In addition, since the designed inverted pyramid micro-discharger has two feature sizes of 50 μm and 100 μm, and the groove depths are about 35 μm and 70 μm, respectively, the existence of deep grooves increases its technological difficulty.

The imidization of polyamic acid must be completed at a temperature at which the molecular chain can move, that is, it should be above the peeling transition temperature (Tg) (As shown in Table 3). Therefore, with the progress of the cyclization reaction, the rigidity of the polymer molecular chain becomes higher and higher, and the temperature required to continue imidization also increases accordingly.

Incomplete imidization will lead to the cracking of the PI film. The thermal cyclization is carried out by means of step heating, and a slow temperature rise rate is used to fully volatilize the solvent inside the PI film. This practice prevents internal stress and defects in the PI film, thereby optimizing the effect of imidization. The thermal cyclization conditions were 80°C/30 min, 150°C/60 min, 180°C/30 min, 250°C/60 min, 300°C/30 min, and the heating rate was 2°C/min. In the experiment, the silicon wafer with 100 crystal orientation was selected as the substrate.

The limitation of etching power greatly reduces the maskless etching rate of plasma PI, and the efficiency is relatively low. In order to improve the etching rate, it can be optimized from two aspects of gas flow and gas composition. The etching gas flow affects the working gas pressure and etching rate [22].

Figure 7 shows the relationship between etching rate and working pressure, oxygen content, and SF6 content. When the power is 60 w, with the increase of oxygen flow, the working pressure gradually increases, and the etching rate increases first and then tends to be saturated. When the flow rate is 60 sccm, a higher etching rate of 145 nm/min can be obtained. This is because the gas flow rate is small, and the particle density in the vacuum chamber is small, so the working pressure is small, the probability of electrons and oxygen molecules colliding is small, the generation of active ions is small, and the physical sputtering and chemical reaction etching effects are weak. With the increase of the flow rate, the particle density in the vacuum chamber gradually increases, and the air pressure also increases, and the glow discharge excites more active ions, which greatly enhances the physical and chemical etching effects, so the etching rate increases [23]. However, since the etching power is constant, the active ions that can be excited by the glow discharge have tended to be saturated when the flow rate continues to increase, so the increase of the etching rate becomes moderate.

4.5. Performance Test of Nanohole Hollow Tip Processing. This section describes the electrical performance testing of tiny plasma reactors for nanopore tip processing. Then, the effects of filling gas pressure, power excitation, and external resistance on the stability of the prepared nanotips were studied by edge computing, and the best nanofabrication effect was measured.

RETRACTED

Table 3: The imidization parameters of polyamic acid.

	PI-2611	ZKPI-305	ZKPI-800	Ni
Dielectric constant (1 MHz, 0–50%Rh)	2.9	3.2–3.4	3.0–3.4	0
Dielectric breakdown strength (V/μm)	200	250–350	200–350	0
Thermal expansion coefficient (ppm)	3	30–35	3–4	13
Internal stress(10 μm) (MPa)	2	30–35	0	0
Elongation at break (%)	100	10–20	20–30	0
Glass transition temperature	360	260–280	360	0

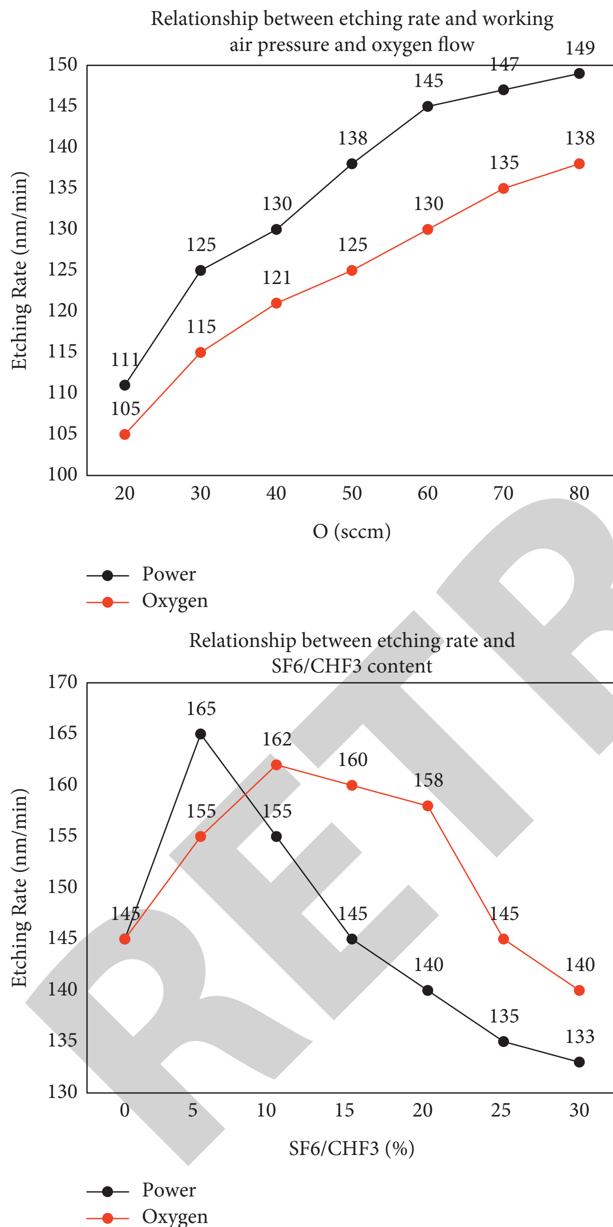

Figure 7: Relationship between etching rate and working pressure, oxygen content, and SF6 content. (a) Relationship between etching rate and working air pressure and oxygen flow. (b) Relationship between etching rate and SF6/CHF3 content.

First, slowly increase the power supply voltage, the voltmeter at both ends of the arrester is close to the supply voltage, and the ammeter in the path is almost zero, that is, the resistance of the micro-arrestor is very large, which can be considered as an insulator. When the voltage increases to a certain value (~500 V), the voltage across the micro-discharger drops instantaneously and the ammeter shows a higher value. When the air pressure is low, the density of electrons and particles in the vacuum chamber is low, and sufficient collision cannot occur, so a larger external electric field is required to enhance the energy of the particles and increase the collision between the particles. As the gas pressure increases, the cathode drop length decreases, the plasma is more concentrated at the hollow cathode, the diffusion loss decreases, and the beam electron penetration decreases, which can then be effectively stopped. Corresponding to Table 4, it can be seen that the SF6 breakdown discharge parameters measured here conform to the variation law of gas discharge conditions.

The breakdown potential is related to the type of gas. The discharge characteristics of the micro-discharger in Ar were also tested for comparison. Figure 8 shows the breakdown voltage versus gas pressure for Ar and SF6. When SF6 discharges, with the increase of air pressure, the breakdown voltage of the arrester first decreases and then increases gradually. It is the smallest at 5 kPa and reaches the optimal 490 V, at this time (PD) $m = 0.5$ Pa·m. The breakdown voltage of Ar does not change much with the increase of gas pressure, because when the gas pressure is 10 kPa, PD = 1 Pa m, which is close to its minimum breakdown potential (PD) $m = 1.2$ Pa m. The breakdown voltage of Ar is about 380 V, while the breakdown voltage of SF6 is about 100 V higher than that of Ar, which is about 480 V. This is due to the influence of the ionization potential of the gas on the breakdown potential: other things being equal, the greater the ionization potential of the gas, the greater the breakdown potential. Ar reaction ionization potential (15.76 eV) and excitation potential (11.53 eV, 11.72 eV) are lower than the splitting potential (≥16 eV) of SF6, fewer particles, and more electrons are generated for re-collision to generate more ionization. However, there are more SF6 reactive particles, and the collision loss of electrons with these ions and neutral particles is huge. During plasma discharge, the Ar discharge voltage is also much higher than that of SF6.

Plasma microdischargers have high resistance before breakdown discharge and can be considered insulators. When the source voltage is increased to the breakdown voltage of the arrester, the gas breakdown of the arrester will form an initial conduction current, and both ends of the power supply will become the initial point-to-point voltage [24]. Keeping the power supply voltage at the time of breakdown, the voltage across the arrester changes abruptly,

RETRACTED

Table 4: SF6 breakdown discharge parameters.

Gas	Quality score	V_{sm}	PD (pa.cm)	P (kPa)/100 μm
H_2	2	273	153.3	15.3
N_2	28	251	89.3	8.93
SH_4	36	414	80.0	8
CO_2	44	420	68.0	6.8
SO_2	64	457	44.0	4.4
SF_6	146	513	30	3
Ar	40	137	120	12

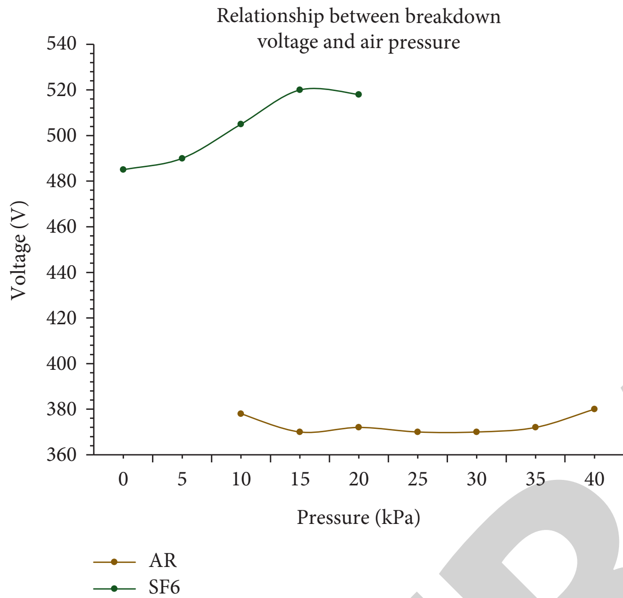

Figure 8: Ar and SF6 breakdown voltage versus gas pressure.

and the current and voltage change in the opposite direction during the discharge process, the micro arrester can be equivalent to:

$$V = IR_0 + V_s, \tag{16}$$

wherein V and I are the discharge voltage and discharge current, respectively, R_0 is the negative resistance formed by the discharger during discharge, and V_s is the threshold voltage required to maintain the plasma discharge, that is, the breakdown voltage. According to the formula, the voltage V of the arrester suddenly drops to a certain value after the breakdown. After the gas discharge is maintained for a period of time, the current drops to zero, and the discharge is terminated. If the source voltage is increased again to trigger, the discharge can occur again. It can be seen that the characteristics of discharge are mainly related to breakdown potential and external resistance. The breakdown potential determines the maximum discharge voltage, while the external resistance determines the slope of the discharge curve. Since the supply voltage satisfies:

$$V_i = V + IR_c = I\left(R_0 + R_c\right) + V_s. \tag{17}$$

The supply voltage is therefore the breakdown voltage required for discharge to occur. After the gas breakdown, the self-sustained discharge is maintained for a period of time and the current drops to zero and the discharge is terminated.

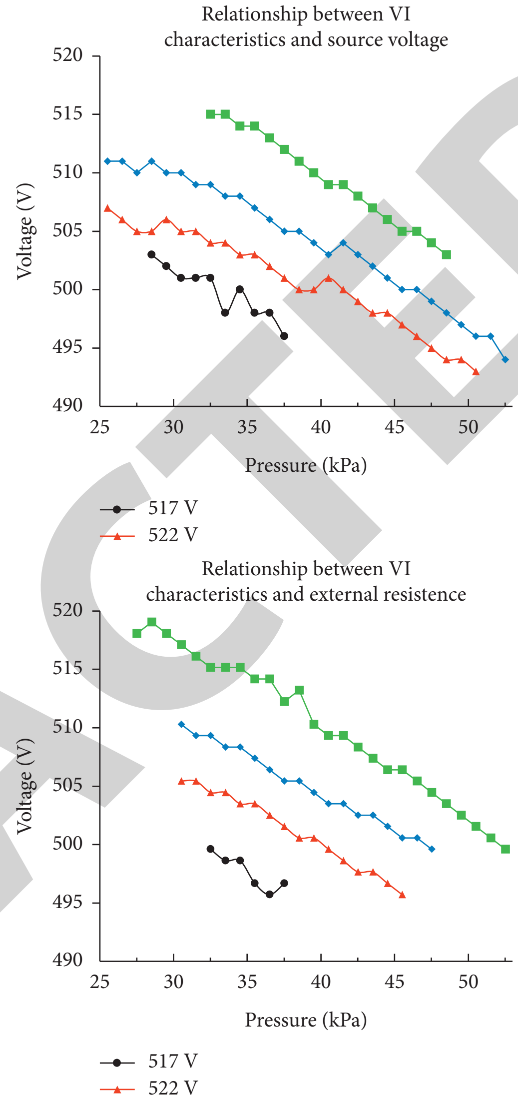

Figure 9: Relationship between characteristic curve and source voltage and external voltage. (a) Relationship between VI characteristics and source voltage. (b) Relationship between VI characteristics and external resistance.

Figure 9 reflects the VI characteristics of a 50 μm inverted pyramid discharger when discharged at different source voltages in 10 kPa SF6. It can be seen that during discharge, as the source voltage increases, the breakdown voltage of the arrester increases, and the discharge voltage also increases under the same discharge current, that is, the discharge curve moves upward, the range has been slightly moved up from 500–505 to below 520 to above 500. Under a certain air pressure, the initial density of particles is the same, and the discharge current does not change much, so the discharge voltage increases significantly, which indicates the volt-ampere characteristics of the micro-discharger under different external resistances. It can be seen from Figure 9 that the breakdown voltages of different external resistance discharges are basically the same when the gas pressure and device size are constant. This also verifies the stability of the prepared nanopore hollow tip from the side.

RETRACTED

RETRACTED

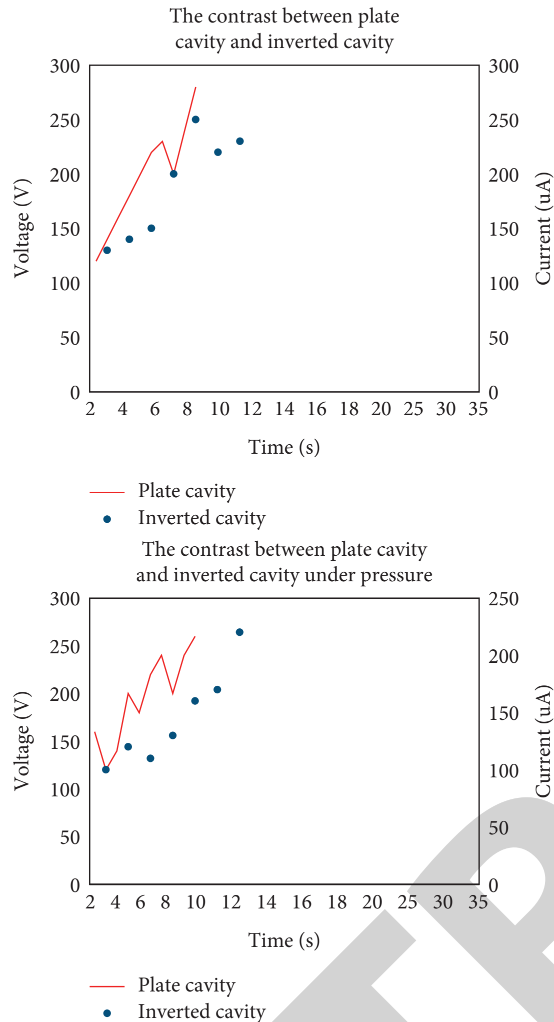

Figure 10: The relationship between the discharge voltage, current and time of the micro-discharger. (a) Contrast between plate cavity and inverted cavity. (b) Contrast between plate cavity and inverted cavity under pressure.

Figure 10 reflects the relationship between the discharge voltage, current and discharge time of the planar and inverted pyramid microdischargers. Due to the continuation of time, the high-energy particles and the wall are neutralized. Therefore, the ion concentration is gradually smaller, it becomes very sparse between 200 and 250, the discharge current gradually decreases, and according to the gradual increase of the discharge voltage, it increases from 100 to 300, which is close to the peak value. After the gas breakdown discharge of the micro-discharger with a flat structure, a certain concentration of ions is generated to form a self-sustaining discharge. It can be maintained by the secondary electron emission generated by the bombardment of the cathode by positive ions, resulting in a gradual increase in the equivalent resistance of the discharger. Inverted pyramid micro-discharger is a type of hollow cathode discharge. After the gas breakdown discharge, on the one hand, high-energy particles bombard the cathode to generate secondary electrons; on the other hand, due to the hollow cathode effect, electrons oscillate repeatedly in the opposite hollow cathode and collide with particles to generate more charged ions and electrons. Therefore, the discharge current gradually increases, and the discharge voltage gradually decreases according to the formula, and the resistance of the discharger gradually decreases.

5. Conclusions

This study first introduces the composition, construction method, and operation principle of the plasma maskless etching system for the preparation of nanohole hollow tips. Then, the effects of filling gas pressure, power excitation, external resistance and other factors on gas breakdown voltage and discharge stability were studied, and the spectral characteristics of SF6 gas during breakdown were measured. At the same time, the stability of the prepared nano-hollow tip was measured, and the optimal processing effect was obtained after calculating the edge of the complex surface shape of the hollow tip. In the future, the author hopes to be able to prepare the same process materials in more ways to save costs and use them in batch production. At the same time, the author looks forward to expanding the complex surface shape to more than just hollow needle tips, so that the same process can be used to process more different materials, especially machinery or equipment parts that are more important in the industry but are scarce in use.

Data Availability

No data were used to support this study.

Conflicts of Interest

There are no potential conflicts of interest in this study.

Acknowledgments

This work was supported by the Project of Natural Science Foundation of Hunan Province (2021JJ40027), the Scientific Research Project of Hunan Education Department (20B113).

References

[1] M. Wan, "Assessment of Cl 2/CHF 3 mixture for plasma etching process on barc and tin layer for 0.21 m metal line: silterra case study," *Turkish Journal of Computer and Mathematics Education (TURCOMAT)*, vol. 12, no. 4, pp. 231–239, 2021.

[2] S. Shimizu, H. Tanabe, M. Yasuda, Y. Hirai, and H. Kawata, "Fabrication of nickel plasma etching mask by nano-imprint lithography and electroless plating," *Journal of Photopolymer Science and Technology*, vol. 33, no. 5, pp. 551–556, 2020.

[3] H. Wang, L. Liu, H. Wang, and J. Zhou, "Control of defects in the deep drawing of tailor-welded blanks for complex-shape automotive panel," *International Journal of Advanced Manufacturing Technology*, vol. 119, no. 5-6, pp. 3235–3245, 2022.

[4] A. V. Sosin, D. A. Sidorenko, and P. S. Utkin, "Numerical study of the interaction of a shock wave with moving rotating

bodies with a complex shape," *Computer Research and Modeling*, vol. 13, no. 3, pp. 513–540, 2021.
[5] Z. C. Tang, Z. J. Fu, and C. S. Chen, "A localized MAPS using polynomial basis functions for the fourth-order complex-shape plate bending problems," *Archive of Applied Mechanics*, vol. 90, no. 10, pp. 2241–2253, 2020.
[6] P. Kochovski and V. Stankovski, "Supporting smart construction with dependable edge computing infrastructures and applications," *Automation in Construction*, vol. 85, pp. 182–192, 2018.
[7] T. X. Tran, A. Hajisami, P. Pandey, and D. Pompili, "Collaborative mobile edge computing in 5G networks: new paradigms, scenarios, and challenges," *IEEE Communications Magazine*, vol. 55, no. 4, pp. 54–61, 2017.
[8] D. H. Park, H. I. Jeong, S. W. Kim, and C. M. Lee, "Shape optimization for lightweight of the line center for processing complex shape parts," *The Korean Society of Manufacturing Process Engineers*, vol. 20, no. 8, pp. 86–92, 2021.
[9] V. A. Che, J. Yang, and Z. Yu, "Analysis on micro complex shape via hole punching on low temperature Co-fired ceramics[J]," *New Journal of Glass and Ceramics*, vol. 10, no. 1, pp. 1–13, 2020.
[10] L. Chen, L. Xu, K. Wang, B. Li, and J. Hong, "Parametric structural optimization of 2D complex shape based onIsogeometric analysis," *Computer Modeling in Engineering and Sciences*, vol. 124, no. 1, pp. 203–225, 2020.
[11] L. Zhi, W. M. Wang, L. Guo, L. Liu, and G. Q. Huang, "Toward open manufacturing: a cross-enterprises knowledge and services exchange framework based on blockchain and edge computing[J]," *Industrial Management & Data Systems*, vol. 118, no. 9, pp. 303–320, 2018.
[12] T. Taleb, S. Dutta, A. Ksentini, M. Iqbal, and H. Flinck, "Mobile edge computing potential in making cities smarter," *IEEE Communications Magazine*, vol. 55, no. 3, pp. 38–43, 2017.
[13] T. Q. Dinh, J. Tang, Q. D. La, and T. Q. S. Quek, "Offloading in mobile edge computing: task allocation and computational frequency scaling," *IEEE Transactions on Communications*, vol. 65, no. 8, pp. 3571–3584, 2017.
[14] Q. Yuan, H. Zhou, J. Li, Z. Liu, F. Yang, and X. S. Shen, "Toward efficient content delivery for automated driving services: an edge computing solution," *IEEE Network*, vol. 32, no. 1, pp. 80–86, 2018.
[15] X. Chen, Q. Shi, L. Yang, and J. Xu, "ThriftyEdge: resource-efficient edge computing for intelligent IoT applications," *IEEE Network*, vol. 32, no. 1, pp. 61–65, 2018.
[16] R. Wang, J. Yan, D. Wu, H. Wang, and Q. Yang, "Knowledge-centric edge computing based on virtualized D2D communication systems," *IEEE Communications Magazine*, vol. 56, no. 5, pp. 32–38, 2018.
[17] B. P. Rimal, D. P. Van, and M. Maier, "Mobile-edge computing versus centralized cloud computing over a converged FiWi access network," *IEEE Transactions on Network & Service Management*, vol. 14, no. 3, pp. 498–513, 2017.
[18] M. Gusev and S. Dustdar, "Going back to the roots—the evolution of edge computing, an IoT perspective," *IEEE Internet Computing*, vol. 22, no. 2, pp. 5–15, 2018.
[19] F. Qiang and N. Ansari, "Application aware workload allocation for edge computing based IoT[J]," *IEEE Internet of Things Journal*, vol. 5, no. 3, pp. 2146–2153, 2018.
[20] L. Hong, Y. Zhang, and Y. Tao, "Blockchain-enabled security in electric vehicles cloud and edge computing[J]," *IEEE Network*, vol. 32, no. 3, pp. 78–83, 2018.
[21] K. Zhang, S. Leng, Y. He, S. Maharjan, and Y. Zhang, "Cooperative content caching in 5G networks with mobile edge computing," *IEEE Wireless Communications*, vol. 25, no. 3, pp. 80–87, 2018.
[22] Z. Zhou, H. Liao, B. Gu, K. M. S. Huq, S. Mumtaz, and J. Rodriguez, "Robust mobile crowd sensing: when deep learning meets edge computing," *IEEE Network*, vol. 32, no. 4, pp. 54–60, 2018.
[23] X. Xu, J. Liu, and X. Tao, "Mobile edge computing enhanced adaptive bitrate video delivery with joint cache and radio resource allocation," *IEEE Access*, vol. 5, no. 99, pp. 16406–16415, 2017.
[24] R. Ju, P. Yi, A. Goscinski, and R. A. Beyah, "Edge computing for the internet of things," *IEEE Network*, vol. 32, no. 1, pp. 6-7, 2018.

RETRACTED